nanomaterials

MDPI

Article

Development of Hydroxyapatite Coatings for Orthopaedic Implants from Colloidal Solutions: Part 2—Detailed Characterisation of the Coatings and Their Growth Mechanism

Bríd Murphy [1,2,*], Mick A. Morris [1,2,*] and Jhonattan Baez [1,2]

[1] Advanced Materials & Bioengineering Research Centre (AMBER), Trinity College Dublin, D02 CP49 Dublin 2, Ireland; baezj@tcd.ie
[2] School of Chemistry, Trinity College Dublin, D02 PN40 Dublin 2, Ireland
* Correspondence: murphb52@tcd.ie (B.M.); morrism2@tcd.ie (M.A.M.)

Abstract: This study is the second part of a two-part study whereby supersaturated solutions of calcium and phosphate ions generate well-defined hydroxyapatite coatings for orthopaedic implants. An 'ideal' process solution is selected from Part 1, and the detailed characterisation of films produced from this solution is undertaken here in Part 2. Analysis is presented on the hydroxyapatite produced, in both powder form and as a film upon titanium substrates representative of orthopaedic implants. From thermal analysis data, it is shown that there is bound and interstitial water present in the hydroxyapatite. Nuclear magnetic resonance data allow for the distinction between an amorphous and a crystalline component of the material. As hydroxyapatite coatings are generated, their growth mechanism is tracked across repeated process runs. A clear understanding of the growth mechanism is achieved though crystallinity and electron imaging data. Transmission electron imaging data support the proposed crystal growth and deposition mechanism. All of the data conclude that this process has a clear propensity to grow the hydroxyapatite phase of octacalcium phosphate. The investigation of the hydroxyapatite coating and its growth mechanism establish that a stable and reproducible process window has been identified. Precise control is achieved, leading to the successful formation of the desired hydroxyapatite films.

Keywords: hydroxyapatite; solution deposition; novel coating; deposition kinetics; functional coatings; structural characterizations

check for updates

Citation: Murphy, B.; Morris, M.A.; Baez, J. Development of Hydroxyapatite Coatings for Orthopaedic Implants from Colloidal Solutions: Part 2—Detailed Characterisation of the Coatings and Their Growth Mechanism. *Nanomaterials* **2023**, *13*, 2606. https://doi.org/10.3390/nano13182606

Academic Editors: Zhuohong Yang and Zhuangzhuang Chu

Received: 14 August 2023
Revised: 12 September 2023
Accepted: 19 September 2023
Published: 21 September 2023

Copyright: © 2023 by the authors. Licensee MDPI, Basel, Switzerland. This article is an open access article distributed under the terms and conditions of the Creative Commons Attribution (CC BY) license (https://creativecommons.org/licenses/by/4.0/).

1. Introduction

The coating of metal titanium alloy implants (or other metals such as chromium cobalt) is key to improving the bodily response to a metal. As mentioned in Part 1 [1] of this study, hydroxyapatite (HA) coatings on orthopaedic implants mitigate fibrous build-up and promote implant fixation [2,3]. In this, Part 2 of the study, the evolution of HA as it grows on a substrate and the resulting film is extensively characterised. How HA film emerges with different mechanical properties from any coating process depends on many parameters, such as temperature, pressure and process time [4–6]. Similarly, HA will grow differently based on its precursors, be they synthetic or biologically derived; for example, mammalian or shell-derived HA can have variations in particle size or phase composition [7,8]. HA film will have different crystallinity based on its substrate chemistry [9–11]. Some methods of HA coating also incur water content which requires dehydration [12,13]. The interaction and the outcome between all these process parameters and the eventual film formed vary greatly by coating process.

There are many industrial techniques for HA coating, such as plasma spraying, chemical vapour deposition, electrochemical deposition, sol-gel deposition or ion assisted deposition, that can be used to form HA coatings on a surface. Within any synthetic process

different calcium phosphate (Ca-P) phases can be created: amorphous calcium phosphate (ACP), α/β-tricalcium phosphate (α/β-TCP), octacalcium phosphate (OCP) or pure HA [14]. These other Ca-P phases have reabsorption and dissolution rates in vivo that differ from HA, thus affecting coating performance [15–19]. HA coatings must be sufficiently porous to encourage protein and mineral deposition in order to form new bone at the site [20–24].

The most common industrial HA coating techniques, plasma spraying and electrochemical deposition, have poor porosity control, poor crystalline phase control, require expensive tools (high temperatures or currents) and have poor coating adhesion [25]. Plasma spraying produces sub-micron needles and plates within micron-sized lamellae which allows for a porous structure [26,27]. Plasma spraying induces the less desirable α/β-TCP and relies upon post-deposition heating to crystalize the HA, which can result in low porosity [28,29]. Electrochemical HA coating deposits may sometimes suffer from defects in the coatings taking the form of certain Ca-P phases or hydrogen bubbles [30,31]. Sol-gel and biomimetic methods are commonly used in hydroxyapatite coating research [32]. Sol-gel processes can include elastic, part-polymer and ceramic composite materials which are useful to study the repair of bone cartilage [33–35]. Biomimetic processes using simulated bodily fluids have been studied as a means to grow HA on a surface [36,37]. Sol-gel deposited HA coatings have the highest coating adhesion of all methods, whereas biomimetic HA coating is the closest in nature to the body's endogenous bone growth pathway [32,38]. Sol-gel and biomimetic processes are hindered by time-consuming steps and, in the case of biomimetic processes, rely heavily on the use of simulated body fluid [39–42].

Poor porosity and thickness control, along with poor substrate adhesion, are some of the unfavourable attributes of existing HA coating methods [43]. The advantages of existing methods lie within their mechanical properties and their easy affinity for titanium surfaces [44].

As outlined in Part 1 of this paper, this method of depositing hydroxyapatite (HA) on orthopaedic implant-type substrates, using saturated solutions of calcium and phosphorous, has the benefits of sol-gel techniques and biomimetic techniques. Coating crystallisation occurs at low temperatures, unlike in other methods. This process entices HA to grow in a self-assembling manner, encouraging high porosity and strict phase control. Part 1 of this paper provides us with an ideal process solution, process time and process temperature at which to grow hydroxyapatite coatings from solution. The formation of HA at surfaces is not well understood; the focus of research has mainly been on characterisation rather than the mechanism of film formation.

Further work is carried out herein on the mechanism of film formation upon a titanium alloy surface. Through thermal analysis, nuclear magnetic resonance (NMR), X-ray diffraction (XRD) and transmission electron microscopy (TEM), we identify the initial nucleation of Ca-P through to the final film characteristics. Once surface coating has commenced, XRD is performed at different stages of the process to identify each phase's composition and how they emerge during the process. By proving the repeatable and reliable physiochemical outcomes of this process, a new generation of HA coatings can be engineered, ultimately improving patient prognoses post-implantation.

2. Materials and Methods

All materials and reagents were used as received. Monobasic potassium phosphate (KH_2PO_4) United States Pharmacopeia (USP) reference standard, Honeywell Fluka hydrochloric (HCl) acid solution 6 M, tris(hydroxymethyl)-aminomethane (TRIS) ACS reagent, 99.8% sodium chloride (NaCl) BioXtra and 99.5% calcium nitrate tetrahydrate ($Ca(NO_3)_2{\cdot}4H_2O$) ACS reagent were all from Sigma Aldrich (Wicklow, Ireland). A calibrated benchtop pH meter with a temperature enabled probe (Orion Star A111, [Thermo Scientific™, Loughborough, UK]) was used for pH measurements with an accuracy of 0.001 pH. Titanium coupons of Ti-6Al-4V alloy were used as substrates. All substrates were submerged in hot basic solutions to increase roughness and yield a negatively charged surface for the calcium ion attachment [45,46].

KH_2PO_4, TRIS and NaCl were mixed in deionized water (DIW) to yield a supersaturated phosphate concentrate. HCl was added to increase the stability of the concentrate to prevent precipitation. $Ca(NO_3)_2{\cdot}4H_2O$ was mixed with DIW to yield a supersaturated calcium concentrate. For deposition, the supersaturated concentrates were combined before a dilution factor of between 15 and 17 was applied. The process solution was heated to 46 °C. A custom-designed experimental apparatus was used for deposition. A sample holder, thermometer and pH probe for in situ temperature and acidity measurements, and an overhead stirrer to agitate the solution, were inserted into the vessel. High agitation rates of 1000 RPM prevented gross precipitation of the apatite mineral from the solution. Substrates were placed in the reaction vessel for deposition then removed and rinsed with DIW; this process was repeated several times with fresh solutions to grow a coherent layer of HA at the solution–substrate interface. In between process runs, samples were left to dry for a minimum of 15 min in ambient conditions. To facilitate some powder analyses two powders were collected; (i) HA powder was collected by scraping it from surfaces post-solution deposition (for thermal analysis and nuclear magnetic resonance) and (ii) the process solutions underwent evaporation to remove the solvent and the dried solute was collected (for crystallinity analysis).

Solid-state nuclear magnetic resonance spectroscopy (NMR) was performed using a 9.4T Bruker Avance III HD NMR spectrometer equipped with a 3.2 mm H-F/X CP-MAS probe with TopSpin software version 3.6.5 (Bruker, Coventry, UK). The spectra were recorded at a Larmor frequency of 400.13 and 161.97 MHz for ^{1}H and ^{31}P, respectively. Chemical shifts were externally referenced to $NH_4(H_2PO_4)$ and TMS for ^{31}P and ^{1}H, respectively. A powder HA sample was added to a zirconia rotor, which was then spun at a magic angle spinning of 20 kHz. All spectra were run at room temperature. The ^{31}P MAS spectra were measured at a spin rate of 20 kHz and with 50 kHz proton decoupling. An exponential window function of 20 Hz line broadening was applied to each FID before the Fourier transformation. The 2D $^{31}P\{^{1}H\}$ heteronuclear correlation (HETCOR) experiments were run with a contact time (τ_{CP}) of 0.5 ms and a recycling delay of 8 s at 20 °C. Thermogravimetric analysis (TGA) was carried out using Perkin Elmer Pyris 1 TGA; samples were held at 30 °C for 15 min and then heated from 30 °C to 900 °C at 10.00 °C min^{-1}. DSC was carried out using the Perkin Elmer Diamond DSC 800; the sample was heated from 20 °C to 500 °C at 10.00 °C min^{-1}, held for 1.0 min at 500 °C before cooling to 20 °C at 100 °C min^{-1}, held for 5.0 min at 20 °C and reheated to 500 °C at 10.00 °C min^{-1}. However, it is the first heating which is reported on. X-ray Diffraction (XRD) patterns were acquired using a Bruker Advance Powder Diffractometer (Cu-Kα radiation with λ = 1.5406 Å, an operating voltage of 40 kV and a current of 40 mA). Measurements were performed in the 2θ range from 10° to 60° with steps of 0.004°. XRD diffractograms of HA powder from the dried process solution and HA films, after two, four and seven deposition runs, were collected. XRD was also performed on the blank titanium substrate. Scanning Electron Microscope (SEM) images were recorded using a Zeiss Ultra Plus system with the accelerating voltage of 5 kV, at a working distance between 3 and 10 mm and using an in-lens detector or secondary electron detector.

Lamellae for TEM cross-section images were prepared on a Zeiss AURIGA Focused Ion Beam (FIB), with accelerating voltages of 5–30 kV and ion beam currents of 50 pA–2 nA. Transmission Electron Microscopy (TEM) coupled with EDX analyses were performed on a FEI Titan 80–300 microscope with a Schottky-type field emission electron gun operated at 300 kV and a Bruker XFlash 6T-30 detector (resolution 129 eV).

3. Results

3.1. Analysis of HA Generated from within This Process in Powder Form

Powder analysis was performed on apatite mineral to understand how phases emerge within solution and upon solution–surface interaction. TGA analysis of this HA powder revealed the presence of adsorbed water and interstitial water, similar to other HA studies [47–49]. In the TGA data, Figure 1a showed a 4% weight loss by 600 °C at a steady rate.

From 0 °C to 200 °C the weakly adsorbed water loss was ~2%. This was accompanied by a large heat flow in the DSC data (Figure 1b). Figure 1b showed a large peak at 113 °C which corresponded to a change in enthalpy of 101.2 Jg^{-1}. The TGA data showed a decrease in mass from 200 °C to 400 °C likely due to chemically bound water loss of ~2%. Again, this was accompanied by a significant heat flow, shown in the DSC data by a smaller peak at 368 °C, which corresponded to a change in enthalpy of 29.7 Jg^{-1}. There was no sign of phosphate decomposition, which only occurs significantly at temperatures >600 °C. The TGA analysis of HA compounds commonly show a weight gain at 700 °C upwards; this is a bounce back in weight due to the recrystallization of the mineral and it is seen in Figure 1a [50,51].

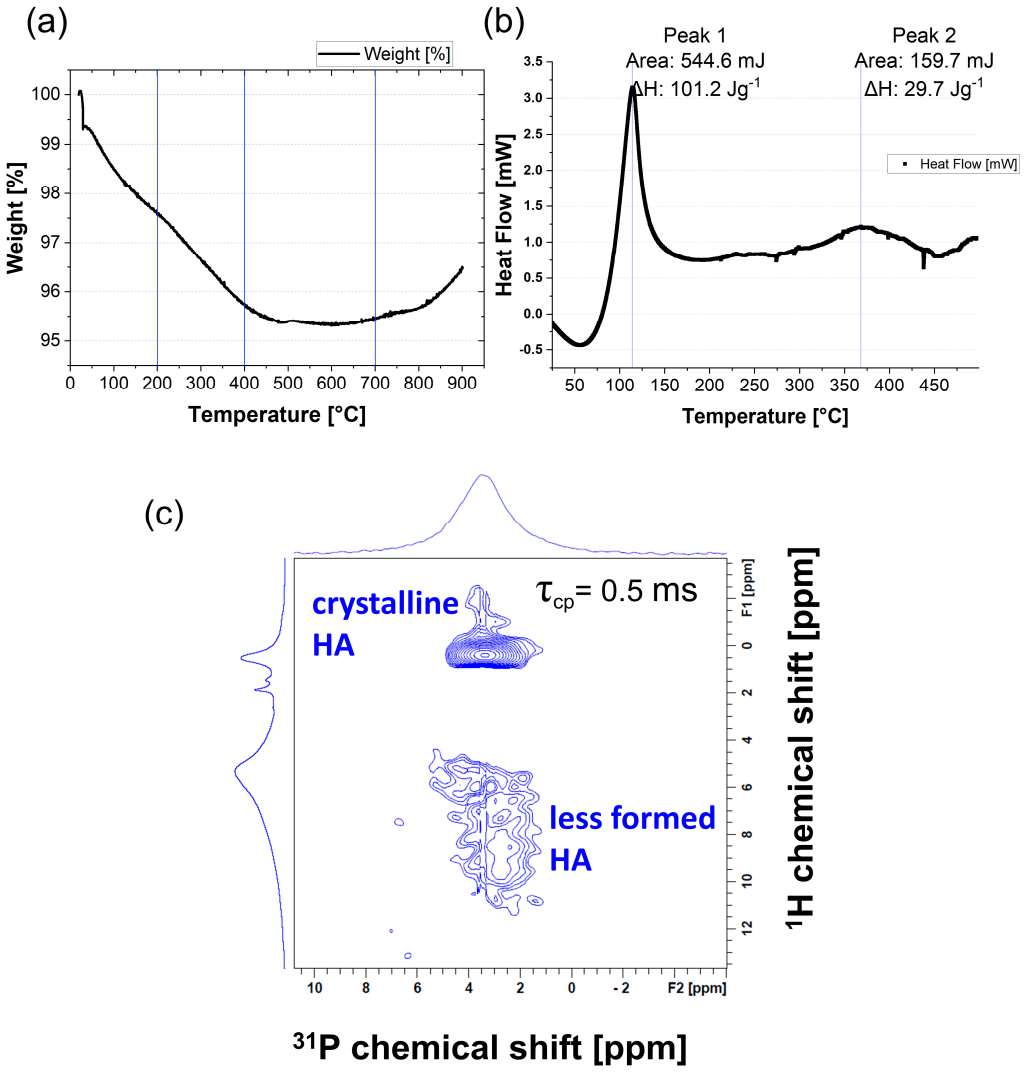

Figure 1. (**a**) Thermogravimetric data (TGA) showing weight loss as percentage loss from the samples versus temperature, (**b**) differential scanning calorimetry (DSC) data for the first heating of a sample, graph of heat flow (mW) versus temperature, (**c**) solid-state nuclear magnetic resonance 2D heteronuclear correlation sequence (NMR 2D HETCOR) measuring cross-polarisation of ^{1}H and ^{31}P proton spectra at a relaxation time (τ) of 0.5 ms, showing two distinct peak regions as blue contours.

Solid-state NMR of HA powder was performed and the 1D spectra of ^{1}H and ^{31}P were collected (Supplemental Figures S1 and S2). The 1D spectra gave little information about the hydration state of the phosphorous species because of low resolution. However, 2D heteronuclear correlation (2D HETCOR) experiments which correlated ^{1}H chemical shifts with ^{31}P (or other X-nuclei) chemical shifts provided excellent ^{1}H resolution in the indirect dimension (Figure 1c). Cross-polarisation dynamics are different for ACP versus crystalline

HA, due to different proton pair correlations [52–54]. ACP is correlated by the proton in water with the P proton of a phosphate: $^{1}\mathbf{H}_2O \boxed{\leftrightarrow} {}^{31}\mathbf{P}O_4{}^{3-}$. Crystalline HA material is correlated by the proton of the hydroxyl functional group with the P proton of a phosphate $O^{1}\mathbf{H} \boxed{\leftrightarrow} {}^{31}\mathbf{P}O_4{}^{3-}$. Two distinct areas could be seen on the HETCOR spectrum (τ_{cp} = 0.5 ms) through contour vectors at the location of the cross peaks (Figure 1c). The cross-correlated peak at ^{1}H 0 ppm was due to apatitic OH^- and can be assigned to a more well-formed crystalline HA. The broader cross peak between ^{1}H 5 and 10 ppm was due to correlations between hydrogen phosphates, ACP and free and bound water, i.e., less well-formed HA. The NMR data indicated the existence of two distinct types of HA within the powder, one crystalline and one amorphous. The ACP peak also manifested the presence of water nuclei in and around all HA phases.

3.2. The Growth Mechanism of HA Film on a Titanium Substrate

Films were also analysed in situ to identify relationships between the properties of the solution and the films formed, plus characterisation of the film itself.

To identify the specific crystalline phases of HA present, extensive XRD analysis was performed (Figure 2a and tabulated in Table 1).

Table 1. Peak assignment of peaks seen in X-ray diffraction (XRD) diffractograms in Figure 2a.

Sample	Peak Assignment			
	OCP [002] (26.2°)	**HA [210] (28.5°)**	**HA Triple Peak (32–33°)**	**Titanium (35.8°)**
Dried process solute	Medium	Weak	Strong	Absent
7× runs HA film on Ti	Strong	Weak	Medium	Weak
4× runs HA film on Ti	Strong	Weak	Medium	Medium
2× runs HA film on Ti	Weak	Absent	Strong	Strong
Blank Ti substrate	Absent	Absent	Absent	Strong

The titanium alloy has a strong reflection at a 2θ angle of 35.8°, denoted in Figure 2a as 'Ti'. This titanium peak can be seen on HA coated substrates and the peak decreases in intensity as the number of HA deposition cycles increase [55,56]. There are three peaks of interest in this study with respect to HA [57–62]:

1. OCP [002] is indicative of a calcium deficient plane [002] (26.2°);
2. HA [210] (28.5°);
3. HA Triple Peak containing the planes [211], [112] and [310] in varying degrees and could be masking the present of TCP which would be observed at a similar position.

The powder solute obtained directly from the process solution rather than the substrate gave an XRD pattern which shows amorphous build up around the peaks with a strong indication of triplet for HA. After two process runs, HA film on the substrate shows a weak OCP [002] peak and a strong characteristic HA triplet. This may suggest that the initial attachment could be TCP. After four process runs, the HA layer on the Ti substrate shows a strong OCP [210] peak, the emergence of a HA [210] peak and a broadening of the triplet peak with shoulders implying a mixture of planes. Clearly while HA is forming, the unstable phase of OCP begins to dominate within this solution process. Pure HA can have a peak around 26° but the intensity of it is lower than HA triple peak, unlike in this study where the OCP peak at 26° surpasses the HA triple peak intensity. By the 7th run of HA on the Ti substrate, the OCP [002] peak remains narrow and sharp and rises in intensity relative to the pure HA phases in the diffractogram. This implies that the coating grows preferentially along the [002] calcium-deficient plane within this process [63]. The comparison of diffractograms between HA film on the surfaces and dried HA solute shows that the substrate encourages much sharper peak shapes. This confirms that the presence of a substrate in solution causes heterogenous nucleation and orientation of the crystallites,

with OCP being more prevalent than pure HA. This process could be driven by surface alignment or epitaxy between the substrate and the HA type coating.

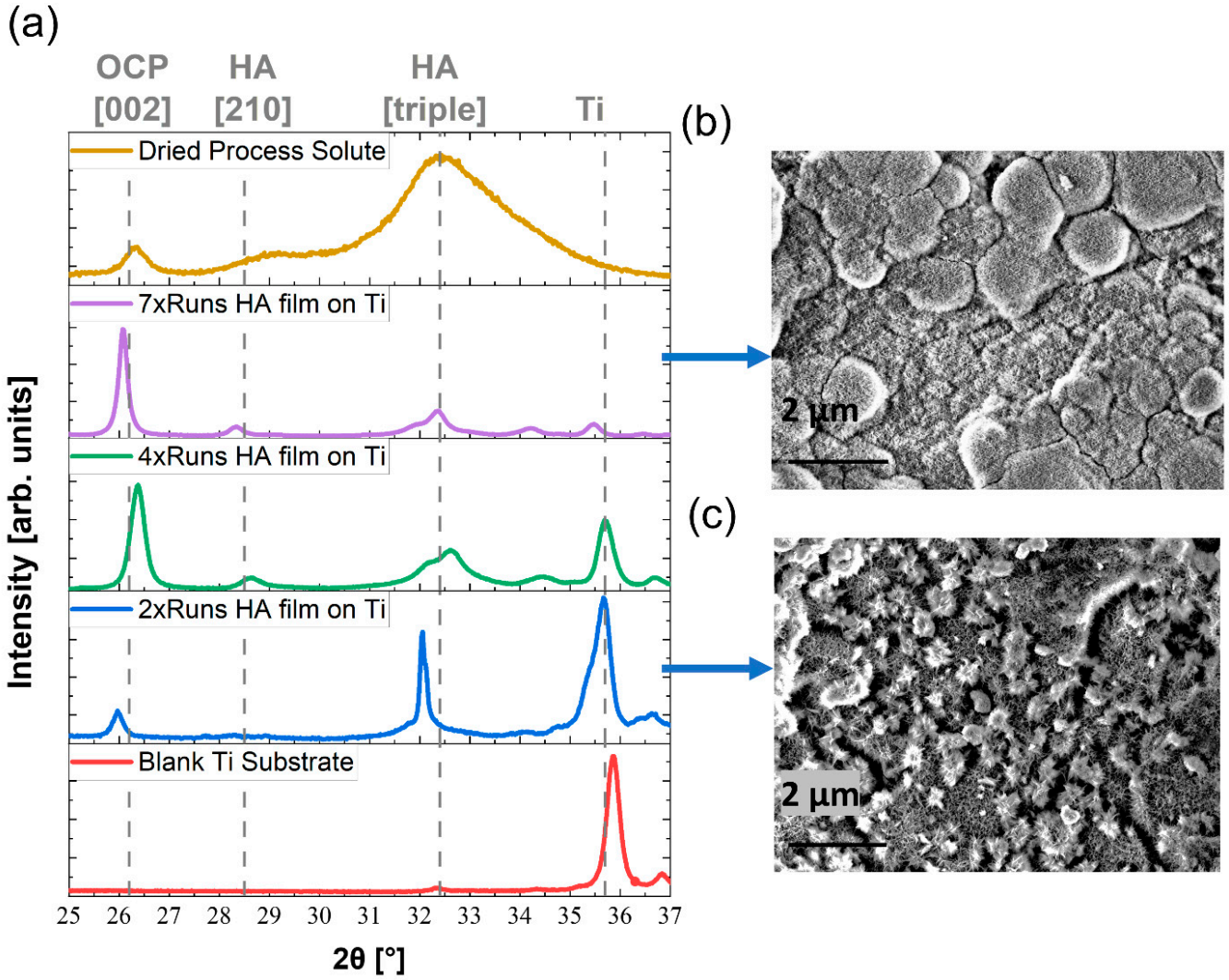

Figure 2. (**a**) X-ray diffraction (XRD) diffractograms in the region of 2θ angle 25° to 37°, with separate trends shown for a blank titanium substrate, films of hydroxyapatite on a titanium substrate after 2, 4 and 7 process runs and a trend from the dried process solute. (**b**) Scanning Electron Microscope (SEM) image of hydroxyapatite film on titanium alloy coupon after 2 hydroxyapatite solution deposition runs (**c**) SEM image of hydroxyapatite film on titanium alloy coupon after 2 hydroxyapatite solution deposition runs.

The SEM images in Figure 2b,c represent the HA film at seven and two process runs, respectively. It is clear that the film develops cobweb-like interconnectivity with the pores, which develop to a full coverage of a porous film after seven process runs. This morphological structure has been shown in various in vitro studies to be the most advantageous HA structure by which to proliferate bone-growth cells [64–66]. As the coverage grows from Figure 2c to Figure 2b, it rationalises the diminishing Ti substrate peak.

It should be noted that OCP, $Ca_8(HPO_4)_2(PO_4)_4 \cdot 5H_2O$, has an apatitic structure with a 'hydrated' water layer along the c axis [67,68]. These repeating OCP crystallites can be assigned to the [002] peak at XRD for our HA films. Correspondingly, our HA films also show the water content in the TGA, DSA and NMR data.

To further analyse the specific planes within the HA film on the titanium substrate, FIB lamellae were cut from the deposited films for cross-sectional TEM analysis. The TEM image indicates a coating thickness of 6 µm (see Figure 3a). Figure 3b–d shows <20 nm segments of

dark and light features, which are thought to be layers of pores developed through the coating process. The dark areas are small nanoparticles, possibly gallium implanted during the FIB sectioning. Figure 3e,f shows crystalline areas circled, suggesting that the coating consists of polycrystalline domains within an amorphous matrix. The HRTEM images (Figure 3g,h) depict areas of high crystallinity with lattice fringes that are highly uniform and perfectly orientated with respect to each other. FFT analysis was performed on crystalline areas (Figure 3i). From the FFT diffractogram, we found the d-spacings of d = 0.344 nm and d = 0.284 nm correspond to the XRD peaks at 26° and 32° and correlate with the XRD data shown in Figure 2a [69,70]. In Figure 3i, strong [002] and [002] reflections are consistent with the XRD data. The absence of the [001] reflection suggests that here is still some of the pure HA phase present, since this phase has a symmetry assignment of $P6_3/m$ where this reflection phase is forbidden [71]. FFT diffractograms were fitted with a CIFfile 1534327, which is a mixture of OCP and HA, using CrystalMaker and CrystalDiffract software and showed excellent alignment (see Supplemental Figure S3).

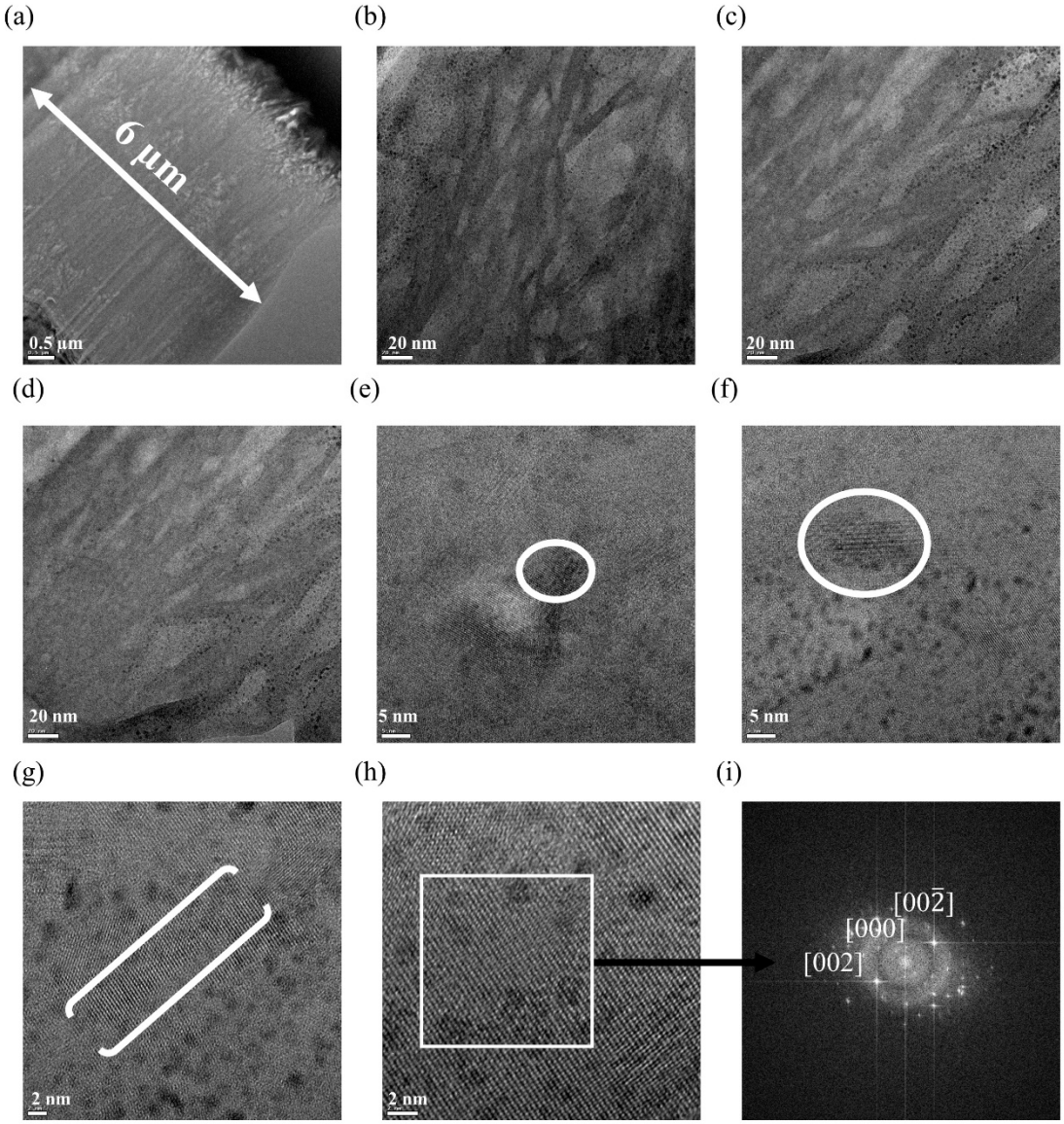

Figure 3. (**a**–**h**) Transmission electron microscope (TEM) images of lamellae cut into HA film over titanium substrate, (**e**–**g**) have areas of high crystallinity outline by white circles or brackets (**i**) fast Fourier transform (FFT) performed on crystalline areas which present in white square in (**h**) to identity lattice parameters.

The crystallinity analysis presented here shows a coating comprising amorphous and distinct crystalline zones. The combination of these phases of ACP, OCP and some pure HA are desired for HA bone cement since these phases stimulate bone reformation in vitro [72,73]. New studies relating to the Mg alloy coatings for orthopaedic implants are also highlighting these ACP, OCP and HA phases as being beneficial for controlled resorption [74,75]. The phases, combined with the morphological structure of our HA coating, confirm that we have designed a process of making highly osteoinductive coatings.

4. Conclusions

This work has proved the efficacy of a coating process whereby an orthopaedic-quality film of hydroxyapatite can be generated at a surface from supersaturated solutions of calcium and phosphate ions. Based on findings in Part 1 of this study, films were generated herein using process solutions of specific concentrations. The subsequent growth of HA was investigated through various characterisation methods. Thermal analysis highlighted a hydrated nature within the HA film grown, which is to be expected from an aqueous process. However, some of the water content can be assigned to hydrated interstitial water content from the OCP phase. The NMR data proved that there are two distinct types of material being formed within this process: amorphous and crystalline.

Crystallinity analysis reveals the specific planes of HA that are present post-deposition. The XRD data show that the present of a substrate alters the formation mechanism and HA on a surface favours growth on the calcium deficient plane of [002] after seven process runs. The SEM data show the comprehensive HA coverage achieved, without compromising on the porosity of the film. The TEM data show that, after seven process runs, the thickness of the coating is 6 μm. The TEM data support that the film is an amorphous layer with crystalline pockets. The FFT analysis of these crystalline pockets show again that both OCP and HA are present through reflection and d-spacing data.

From these results, solution deposition of HA is shown to produce excellent HA coatings on titanium parts. The deposition can be tracked as the coating grows and the phase composition and morphology of the HA generated is advantageous for a low-temperature and -cost process. This body of work highlights that there is a large opportunity here in industrialising methods which have thus far only been used in research.

Supplementary Materials: The following supporting information can be downloaded at: https://www.mdpi.com/article/10.3390/nano13182606/s1. Figure S1: Solid state Nuclear Magnetic Resonance 1D ^{1}H proton spectrum from a standard one pulse sequence at 20 kHz spin rate. Figure S2: Solid state Nuclear Magnetic Resonance 1D ^{31}P (phosphorus) spectrum from a standard one pulse sequence at 20kHz spin rate with 50 kHz decoupling. Figure S3: (A) high magnitude Transmission electron microscope (TEM) image of crystalline area within the deposited HA, insert box of one corner of highly symmetrical lattice fringes (B) Fast Fourier Transform measurement as applied to the highlighted square in A. and (C) Software interface from Single Crystal software (education edition) fitting the crystallographic information file (cif) number 1534327 to the FFT image in C.

Author Contributions: Conceptualization, B.M. and M.A.M.; methodology, B.M. and M.A.M.; investigation, B.M. and M.A.M.; writing—original draft preparation, B.M.; writing—review and editing, J.B. and M.A.M.; visualization, B.M. and J.B.; supervision, M.A.M. All authors have read and agreed to the published version of the manuscript.

Funding: This publication has emanated from research supported in part by a research grant from Science Foundation Ireland (SFI) and is co-funded under the European Regional Development Fund under Grant Number 12/RC/2278 and Grant Number 17/RC-PhD/3477. This research has been co-funded by DePuy Synthes (Ireland).

Data Availability Statement: Data are contained within the article or the Supplementary Material.

Acknowledgments: We thank Lucie Hankey and Aidan Cloonan, for technical advice and scientific discussions. We thank our project manager Niamh Cronly for the advice and guidance throughout all the work we do. We thank Manuel Ruther of the Chemistry department in TCD for NMR, TGA and

DSC data collection, analysis, help and advice. We thank the AML centre for the electron microscopes and especially Raman Bekarevich for TEM analysis support.

Conflicts of Interest: The authors declare no conflict of interest.

References

1. Murphy, B.; Morris, M.A.; Baez, J. Development of Hydroxyapatite Coatings for Orthopaedic Implants from Colloidal Solutions: Part 1—Effect of Solution Concentration and Deposition Kinetics. *Nanomaterials* **2023**, *13*, 2577. [CrossRef]
2. Keyhani, S.; Movahedinia, M.; Vaziri, A.S.; Soleymanha, M.; Vosoughi, F.; Tahami, M.; LaPrade, R.F. Is Posterior Knee Arthroscopy Using Posterior Portals Necessary for Orthopedic Surgeons? The Latest Evidence on Applications and Techniques. *EFORT Open Rev.* **2023**, *8*, 189–198. [CrossRef] [PubMed]
3. Josyula, A.; Parikh, K.S.; Pitha, I.; Ensign, L.M. Engineering Biomaterials to Prevent Post-Operative Infection and Fibrosis. *Drug Deliv. Transl. Res.* **2021**, *11*, 1675–1688. [CrossRef] [PubMed]
4. Guillem-Marti, J.; Cinca, N.; Punset, M.; Cano, I.G.; Gil, F.J.; Guilemany, J.M.; Dosta, S. Porous Titanium-Hydroxyapatite Composite Coating Obtained on Titanium by Cold Gas Spray with High Bond Strength for Biomedical Applications. *Colloids Surf. B Biointerfaces* **2019**, *180*, 245–253. [CrossRef] [PubMed]
5. Ibrahim, A.-R.; Benoit, R.; Suo, X.; Li, X.; Huang, Y.; Ma, G.; Li, J. Ultra-Fast Route to Synthesizing Biogenic Carbonate Hydroxyapatite: Consequence of a High-Pressure Solid-Solid Preparation Technique. *Chem. Eng. Process. Process Intensif.* **2019**, *142*, 107549. [CrossRef]
6. Hussain, M.A.; Ul Haq, E.; Munawar, I.; Maqbool, A.; Saleem, M.; Rafiq, M.A.; Inam, A.; Hakeem, A.S. Influence of Spark Plasma Sintering Temperature and Hydroxyapatite Nanoparticles on Properties of HA Based Functionally Graded Materials for Bone Prosthesis. *Ceram. Int.* **2022**, *48*, 14481–14490. [CrossRef]
7. Varadavenkatesan, T.; Vinayagam, R.; Pai, S.; Kathirvel, B.; Pugazhendhi, A.; Selvaraj, R. Synthesis, Biological and Environmental Applications of Hydroxyapatite and Its Composites with Organic and Inorganic Coatings. *Prog. Org. Coat.* **2021**, *151*, 106056. [CrossRef]
8. Kumar, R.; Mohanty, S. Hydroxyapatite: A Versatile Bioceramic for Tissue Engineering Application. *J. Inorg. Organomet. Polym.* **2022**, *32*, 4461–4477. [CrossRef]
9. Murphy, B.; Baez, J.; Morris, M.A. Characterising Hydroxyapatite Deposited from Solution onto Novel Substrates: Growth Mechanism and Physical Properties. *Nanomaterials* **2023**, *13*, 2483. [CrossRef]
10. Murphy, B.; Baez, J.; Morris, M.A. Characterizing Hydroxyapatite Deposited from Solution onto Novel Substrates in Terms of Growth Mechanism and Physical Chemical Properties. *Mater. Proc.* **2023**, *14*, 34. [CrossRef]
11. Rajkumar, P.; Sarma, B.K. Substrate Dependent Structural Variations of Biomimetic Carbonated Hydroxyapatite Deposited on Glass, Ti and Sputtered ZnO Thin Films. *Mater. Charact.* **2022**, *191*, 112120. [CrossRef]
12. Hua, L.C.; Wang, W.Y.; Swain, M.V.; Zhu, C.L.; Huang, H.B.; Du, J.K.; Zhou, Z.R. The Dehydration Effect on Mechanical Properties of Tooth Enamel. *J. Mech. Behav. Biomed. Mater.* **2019**, *95*, 210–214. [CrossRef]
13. Heimann, R.B. Structural Changes of Hydroxylapatite during Plasma Spraying: Raman and NMR Spectroscopy Results. *Coatings* **2021**, *11*, 987. [CrossRef]
14. Prakasam, M.; Locs, J.; Salma-Ancane, K.; Loca, D.; Largeteau, A.; Berzina-Cimdina, L. Fabrication, Properties and Applications of Dense Hydroxyapatite: A Review. *J. Funct. Biomater.* **2015**, *6*, 1099–1140. [CrossRef]
15. Schröter, L.; Kaiser, F.; Stein, S.; Gbureck, U.; Ignatius, A. Biological and Mechanical Performance and Degradation Characteristics of Calcium Phosphate Cements in Large Animals and Humans. *Acta Biomater.* **2020**, *117*, 1–20. [CrossRef] [PubMed]
16. Zhou, H.; Yang, L.; Gbureck, U.; Bhaduri, S.B.; Sikder, P. Monetite, an Important Calcium Phosphate Compound–Its Synthesis, Properties and Applications in Orthopedics. *Acta Biomater.* **2021**, *127*, 41–55. [CrossRef] [PubMed]
17. Bohner, M.; Santoni, B.L.G.; Döbelin, N. β-Tricalcium Phosphate for Bone Substitution: Synthesis and Properties. *Acta Biomater.* **2020**, *113*, 23–41. [CrossRef] [PubMed]
18. Liu, D.; Cui, C.; Chen, W.; Shi, J.; Li, B.; Chen, S. Biodegradable Cements for Bone Regeneration. *J. Funct. Biomater.* **2023**, *14*, 134. [CrossRef]
19. Suzuki, O.; Hamai, R.; Sakai, S. The Material Design of Octacalcium Phosphate Bone Substitute: Increased Dissolution and Osteogenecity. *Acta Biomater.* **2023**, *158*, 4742–4753. [CrossRef]
20. Bhat, S.; Uthappa, U.T.; Altalhi, T.; Jung, H.-Y.; Kurkuri, M.D. Functionalized Porous Hydroxyapatite Scaffolds for Tissue Engineering Applications: A Focused Review. *ACS Biomater. Sci. Eng.* **2022**, *8*, 4039–4076. [CrossRef]
21. Awasthi, S.; Pandey, S.K.; Arunan, E.; Srivastava, C. A Review on Hydroxyapatite Coatings for the Biomedical Applications: Experimental and Theoretical Perspectives. *J. Mater. Chem. B* **2021**, *9*, 228–249. [CrossRef] [PubMed]
22. Xiao, D.; Zhang, J.; Zhang, C.; Barbieri, D.; Yuan, H.; Moroni, L.; Feng, G. The Role of Calcium Phosphate Surface Structure in Osteogenesis and the Mechanisms Involved. *Acta Biomater.* **2020**, *106*, 22–33. [CrossRef] [PubMed]
23. Du, M.; Chen, J.; Liu, K.; Xing, H.; Song, C. Recent Advances in Biomedical Engineering of Nano-Hydroxyapatite Including Dentistry, Cancer Treatment and Bone Repair. *Compos. Part B Eng.* **2021**, *215*, 108790. [CrossRef]
24. Kang, S.; Haider, A.; Gupta, K.C.; Kim, H.; Kang, I. Chemical Bonding of Biomolecules to the Surface of Nano-Hydroxyapatite to Enhance Its Bioactivity. *Coatings* **2022**, *12*, 999. [CrossRef]

25. Safavi, M.S.; Walsh, F.C.; Surmeneva, M.A.; Surmenev, R.A.; Khalil-Allafi, J. Electrodeposited Hydroxyapatite-Based Biocoatings: Recent Progress and Future Challenges. *Coatings* **2021**, *11*, 110. [CrossRef]
26. McCabe, A.; Pickford, M.; Shawcross, J. The History, Technical Specifications and Efficacy of Plasma Spray Coatings Applied to Joint Replacement Prostheses. *Reconstr. Rev.* **2016**, *6*, 19–26. [CrossRef]
27. Safavi, M.S.; Etminanfar, M. A Review on the Prevalent Fabrication Methods, Microstructural, Mechanical Properties, and Corrosion Resistance of Nanostructured Hydroxyapatite Containing Bilayer and Multilayer Coatings Used in Biomedical Applications. *J. Ultrafine Grained Nanostruct. Mater.* **2019**, *52*, 1–17. [CrossRef]
28. Guner, A.T.; Meran, C. A Review on Plasma Sprayed Titanium and Hydroxyapatite Coatings on Polyetheretherketone Implants. *Int. J. Surf. Sci. Eng.* **2019**, *13*, 237–262. [CrossRef]
29. Singh, H.; Kumar, R.; Prakash, C.; Singh, S. HA-Based Coating by Plasma Spray Techniques on Titanium Alloy for Orthopedic Applications. *Mater. Today Proc.* **2022**, *50*, 612–628. [CrossRef]
30. Ranjan Dev, P.; Parambil Anand, C.; Samuvel Michael, D.; Wilson, P. Hydroxyapatite Coatings: A Critical Review on Electrodeposition Parametric Variations Influencing Crystal Facet Orientation towards Enhanced Electrochemical Sensing. *Mater. Adv.* **2022**, *3*, 7773–7809. [CrossRef]
31. Lissandrello, F.; Magagnin, L. Pulsed Electrochemical Deposition of Calcium Phosphate Coatings for Biomedical Applications. *Trans. IMF* **2023**, *101*, 173–178. [CrossRef]
32. Jaafar, A.; Hecker, C.; Árki, P.; Joseph, Y. Sol-Gel Derived Hydroxyapatite Coatings for Titanium Implants: A Review. *Bioengineering* **2020**, *7*, 127. [CrossRef] [PubMed]
33. Ansari, Z.; Kalantar, M.; Kharaziha, M.; Ambrosio, L.; Raucci, M.G. Polycaprolactone/Fluoride Substituted-Hydroxyapatite (PCL/FHA) Nanocomposite Coatings Prepared by in-Situ Sol-Gel Process for Dental Implant Applications. *Prog. Org. Coat.* **2020**, *147*, 105873. [CrossRef]
34. Chen, H.; Wang, R.; Qian, L.; Liu, H.; Wang, J.; Zhu, M. Surface Modification of Urchin-like Serried Hydroxyapatite with Sol-Gel Method and Its Application in Dental Composites. *Compos. Part B Eng.* **2020**, *182*, 107621. [CrossRef]
35. Sebastin, A.X.S.; Uthirapathy, V. In Vitro Electrochemical Behavior of Sol-Gel Derived Hydroxyapatite/Graphene Oxide Composite Coatings on 316L SS for Biomedical Applications. *ChemistrySelect* **2020**, *5*, 12140–12147. [CrossRef]
36. Tan, B.; Zhao, N.; Guo, W.; Huang, F.; Hu, H.; Chen, Y.; Li, J.; Ling, Z.; Zou, Z.; Hu, R.; et al. Biomimetic Hydroxyapatite Coating on the 3D-Printed Bioactive Porous Composite Ceramic Scaffolds Promoted Osteogenic Differentiation via PI3K/AKT/mTOR Signaling Pathways and Facilitated Bone Regeneration In Vivo. *J. Mater. Sci. Technol.* **2023**, *136*, 54–64. [CrossRef]
37. Jiang, J.; Liu, W.; Xiong, Z.; Hu, Y.; Xiao, J. Effects of Biomimetic Hydroxyapatite Coatings on Osteoimmunomodulation. *Biomater. Adv.* **2022**, *134*, 112640. [CrossRef]
38. Koju, N.; Sikder, P.; Ren, Y.; Zhou, H.; Bhaduri, S.B. Biomimetic Coating Technology for Orthopedic Implants. *Curr. Opin. Chem. Eng.* **2017**, *15*, 49–55. [CrossRef]
39. Baino, F.; Yamaguchi, S. The Use of Simulated Body Fluid (SBF) for Assessing Materials Bioactivity in the Context of Tissue Engineering: Review and Challenges. *Biomimetics* **2020**, *5*, 57. [CrossRef]
40. Suchý, T.; Bartoš, M.; Sedláček, R.; Šupová, M.; Žaloudková, M.; Martynková, G.S.; Foltán, R. Various Simulated Body Fluids Lead to Significant Differences in Collagen Tissue Engineering Scaffolds. *Materials* **2021**, *14*, 4388. [CrossRef]
41. Ghorbani, F.; Zamanian, A.; Behnamghader, A.; Daliri-Joupari, M. Bone-like Hydroxyapatite Mineralization on the Bio-Inspired PDA Nanoparticles Using Microwave Irradiation. *Surf. Interfaces* **2019**, *15*, 38–42. [CrossRef]
42. Wei, G.; Gong, C.; Hu, K.; Wang, Y.; Zhang, Y. Biomimetic Hydroxyapatite on Graphene Supports for Biomedical Applications: A Review. *Nanomaterials* **2019**, *9*, 1435. [CrossRef]
43. Beig, B.; Liaqat, U.; Niazi, M.F.K.; Douna, I.; Zahoor, M.; Niazi, M.B.K. Current Challenges and Innovative Developments in Hydroxyapatite-Based Coatings on Metallic Materials for Bone Implantation: A Review. *Coatings* **2020**, *10*, 1249. [CrossRef]
44. Domínguez-Trujillo, C.; Peón, E.; Chicardi, E.; Pérez, H.; Rodríguez-Ortiz, J.A.; Pavón, J.J.; García-Couce, J.; Galván, J.C.; García-Moreno, F.; Torres, Y. Sol-Gel Deposition of Hydroxyapatite Coatings on Porous Titanium for Biomedical Applications. *Surf. Coat. Technol.* **2018**, *333*, 158–162. [CrossRef]
45. Andrusova, N.N.; Zhavoronok, E.S.; Legon'kova, O.A.; Goncharova, A.S.; Kedik, S.A. Polymer–Mineral Compounds for Cementless Hip Replacement. *Polym. Sci. Ser. D* **2020**, *13*, 68–72. [CrossRef]
46. Sánchez-Bodón, J.; Andrade del Olmo, J.; Alonso, J.M.; Moreno-Benítez, I.; Vilas-Vilela, J.L.; Pérez-Álvarez, L. Bioactive Coatings on Titanium: A Review on Hydroxylation, Self-Assembled Monolayers (SAMs) and Surface Modification Strategies. *Polymers* **2022**, *14*, 165. [CrossRef]
47. Durga, R.; Jimenez, N.; Ramanathan, S.; Suraneni, P.; Pestle, W.J. Use of Thermogravimetric Analysis to Estimate Collagen and Hydroxyapatite Contents in Archaeological Bone. *J. Archaeol. Sci.* **2022**, *145*, 105644. [CrossRef]
48. Ebadipour, N.; Paul, S.; Katryniok, B.; Dumeignil, F. Calcium Hydroxyapatite: A Highly Stable and Selective Solid Catalyst for Glycerol Polymerization. *Catalysts* **2021**, *11*, 1247. [CrossRef]
49. Roque-Ruiz, J.H.; Garibay-Alvarado, J.A.; Medellín-Castillo, N.A.; Reyes-López, S.Y. Preparation of Electrospun Hydroxyapatite-Glass Fibers for Removal of Cadmium (Cd+2) and Lead (Pb+2) from Aqueous Media. *Water Air Soil Pollut.* **2020**, *231*, 497. [CrossRef]

50. Greiner, M.; Rodríguez-Navarro, A.; Schmahl, W.; Kocsis, B.; Grupe, G.; Mayer, K. The Bone Mineral Is Carbonato-Hydro-Apatite and It Transforms into Hydroxyapatite by Heating (Cremation) beyond 700 °C. *Acta Crystallogr. Sect. A Found. Adv.* **2019**, *75*, e199. [CrossRef]
51. Malla, K.P.; Regmi, S.; Nepal, A.; Bhattarai, S.; Yadav, R.J.; Sakurai, S.; Adhikari, R. Extraction and Characterization of Novel Natural Hydroxyapatite Bioceramic by Thermal Decomposition of Waste Ostrich Bone. *Int. J. Biomater.* **2020**, *2020*, e1690178. [CrossRef]
52. Jiang, Y.; Ren, C.; Guo, H.; Guo, M.; Li, W. Speciation Transformation of Phosphorus in Poultry Litter during Pyrolysis: Insights from X-ray Diffraction, Fourier Transform Infrared, and Solid-State NMR Spectroscopy. *Environ. Sci. Technol.* **2019**, *53*, 13841–13849. [CrossRef]
53. Wang, J.; Ren, C.; Li, Z.; Li, W. Two-Dimensional Solid-State NMR Spectroscopy Investigations of Surface Precipitation of Phosphate onto Calcite. *Sci. Total Environ.* **2023**, *890*, 164444. [CrossRef] [PubMed]
54. Klimavicius, V.; Maršalka, A.; Kizalaite, A.; Zarkov, A.; Kareiva, A.; Aidas, K.; Hirschinger, J.; Balevicius, V. Step-by-Step from Amorphous Phosphate to Nano-Structured Calcium Hydroxyapatite: Monitoring by Solid-State 1 H and 31 P NMR and Spin Dynamics. *Phys. Chem. Chem. Phys.* **2022**, *24*, 18952–18965. [CrossRef]
55. Hamza, H.M.; Deen, K.M.; Haider, W. Microstructural Examination and Corrosion Behavior of Selective Laser Melted and Conventionally Manufactured Ti6Al4V for Dental Applications. *Mater. Sci. Eng. C* **2020**, *113*, 110980. [CrossRef] [PubMed]
56. Kaschel, F.R.; Vijayaraghavan, R.K.; Shmeliov, A.; McCarthy, E.K.; Canavan, M.; McNally, P.J.; Dowling, D.P.; Nicolosi, V.; Celikin, M. Mechanism of Stress Relaxation and Phase Transformation in Additively Manufactured Ti-6Al-4V via in Situ High Temperature XRD and TEM Analyses. *Acta Mater.* **2020**, *188*, 720–732. [CrossRef]
57. Gross, K.A.; Petzold, C.; Pluduma-LaFarge, L.; Kumermanis, M.; Haugen, H.J. Structural and Chemical Hierarchy in Hydroxyapatite Coatings. *Materials* **2020**, *13*, 4447. [CrossRef]
58. Li, T.-T.; Ling, L.; Lin, M.-C.; Jiang, Q.; Lin, Q.; Lin, J.-H.; Lou, C.-W. Properties and Mechanism of Hydroxyapatite Coating Prepared by Electrodeposition on a Braid for Biodegradable Bone Scaffolds. *Nanomaterials* **2019**, *9*, 679. [CrossRef]
59. Londoño-Restrepo, S.M.; Millán-Malo, B.M.; del Real-López, A.; Rodriguez-García, M.E. In Situ Study of Hydroxyapatite from Cattle during a Controlled Calcination Process Using HT-XRD. *Mater. Sci. Eng. C* **2019**, *105*, 110020. [CrossRef] [PubMed]
60. Pham, D.Q.; Gangadoo, S.; Berndt, C.C.; Chapman, J.; Zhai, J.; Vasilev, K.; Truong, V.K.; Ang, A.S.M. Antibacterial Longevity of a Novel Gallium Liquid Metal/Hydroxyapatite Composite Coating Fabricated by Plasma Spray. *ACS Appl. Mater. Interfaces* **2022**, *14*, 18974–18988. [CrossRef]
61. Londoño-Restrepo, S.M.; Herrera-Lara, M.; Bernal-Alvarez, L.R.; Rivera-Muñoz, E.M.; Rodriguez-García, M.E. In-Situ XRD Study of the Crystal Size Transition of Hydroxyapatite from Swine Bone. *Ceram. Int.* **2020**, *46*, 24454–24461. [CrossRef]
62. Khan, A.S.; Awais, M. Low-Cost Deposition of Antibacterial Ion-Substituted Hydroxyapatite Coatings onto 316L Stainless Steel for Biomedical and Dental Applications. *Coatings* **2020**, *10*, 880. [CrossRef]
63. Grigoraviciute-Puroniene, I.; Tanaka, Y.; Vegelyte, V.; Nishimoto, Y.; Ishikawa, K.; Kareiva, A. A Novel Synthetic Approach to Low-Crystallinity Calcium Deficient Hydroxyapatite. *Ceram. Int.* **2019**, *45*, 15620–15623. [CrossRef]
64. Vilardell, A.M.; Cinca, N.; Garcia-Giralt, N.; Dosta, S.; Cano, I.G.; Nogués, X.; Guilemany, J.M. In-Vitro Comparison of Hydroxyapatite Coatings Obtained by Cold Spray and Conventional Thermal Spray Technologies. *Mater. Sci. Eng. C* **2020**, *107*, 110306. [CrossRef] [PubMed]
65. Lu, M.; Chen, H.; Yuan, B.; Zhou, Y.; Min, L.; Xiao, Z.; Yang, X.; Zhu, X.; Tu, C.; Zhang, X. The Morphological Effect of Nanostructured Hydroxyapatite Coatings on the Osteoinduction and Osteogenic Capacity of Porous Titanium. *Nanoscale* **2020**, *12*, 24085–24099. [CrossRef] [PubMed]
66. Sun, Y.; Zhang, X.; Luo, M.; Hu, W.; Zheng, L.; Huang, R.; Greven, J.; Hildebrand, F.; Yuan, F. Plasma Spray vs. Electrochemical Deposition: Toward a Better Osteogenic Effect of Hydroxyapatite Coatings on 3D-Printed Titanium Scaffolds. *Front. Bioeng. Biotechnol.* **2021**, *9*, 705774. [CrossRef] [PubMed]
67. Yokoi, T.; Shimabukuro, M.; Kawashita, M. Octacalcium Phosphate with Incorporated Carboxylate Ions: A Review. *Sci. Technol. Adv. Mater.* **2022**, *23*, 434–445. [CrossRef]
68. Hamai, R.; Sakai, S.; Shiwaku, Y.; Anada, T.; Tsuchiya, K.; Ishimoto, T.; Nakano, T.; Suzuki, O. Octacalcium Phosphate Crystals Including a Higher Density Dislocation Improve Its Materials Osteogenecity. *Appl. Mater. Today* **2022**, *26*, 101279. [CrossRef]
69. Nosrati, H.; Sarraf-Mamoory, R.; Ahmadi, A.H.; Canillas, M. Synthesis of Graphene Nanoribbons-Hydroxyapatite Nanocomposite Applicable in Biomedicine and Theranostics. *J. Nanotheranostics* **2020**, *1*, 2. [CrossRef]
70. In, Y.; Amornkitbamrung, U.; Hong, M.-H.; Shin, H. On the Crystallization of Hydroxyapatite under Hydrothermal Conditions: Role of Sebacic Acid as an Additive. *ACS Omega* **2020**, *5*, 27204–27210. [CrossRef]
71. Reyes-Gasga, J.; Martínez-Piñeiro, E.L.; Brès, É.F. Crystallographic Structure of Human Tooth Enamel by Electron Microscopy and X-ray Diffraction: Hexagonal or Monoclinic? *J. Microsc.* **2012**, *248*, 102–109. [CrossRef] [PubMed]
72. Bystrom, J.L.; Pujari-Palmer, M. Phosphoserine Functionalized Cements Preserve Metastable Phases, and Reprecipitate Octacalcium Phosphate, Hydroxyapatite, Dicalcium Phosphate, and Amorphous Calcium Phosphate, during Degradation, In Vitro. *J. Funct. Biomater.* **2019**, *10*, 54. [CrossRef] [PubMed]
73. Lukina, Y.; Bionyshev-Abramov, L.; Kotov, S.; Serejnikova, N.; Smolentsev, D.; Sivkov, S. Carbonate-Hydroxyapatite Cement: The Effect of Composition on Solubility In Vitro and Resorption In Vivo. *Ceramics* **2023**, *6*, 1397–1414. [CrossRef]

74. Mahmud, S.; Rahman, M.; Kamruzzaman, M.; Khatun, H.; Ali, M.O.; Haque, M.M. Recent Developments in Hydroxyapatite Coating on Magnesium Alloys for Clinical Applications. *Results Eng.* **2023**, *17*, 101002. [CrossRef]
75. Zhang, A.-M.; Lenin, P.; Zeng, R.-C.; Kannan, M.B. Advances in Hydroxyapatite Coatings on Biodegradable Magnesium and Its Alloys. *J. Magnes. Alloys* **2022**, *10*, 1154–1170. [CrossRef]

Disclaimer/Publisher's Note: The statements, opinions and data contained in all publications are solely those of the individual author(s) and contributor(s) and not of MDPI and/or the editor(s). MDPI and/or the editor(s) disclaim responsibility for any injury to people or property resulting from any ideas, methods, instructions or products referred to in the content.